Materials Research Letters

ISSN: 2166-3831 (Online) Journal homepage: www.tandfonline.com/journals/tmrl20

Synchrotron-based nano-CT insights into microscale mechanics of sintered copper nanoparticles

Jiajie Fan, Xuyang Yan , Chuantong Chen , Leiming Du , Zichuan Li , Junran Zhang , Willem Van Driel & Guoqi Zhang

To cite this article: Jiajie Fan, Xuyang Yan , Chuantong Chen , Leiming Du , Zichuan Li , Junran Zhang , Willem Van Driel & Guoqi Zhang (25 Apr 2026): Synchrotron-based nano-CT insights into microscale mechanics of sintered copper nanoparticles, Materials Research Letters, DOI: 10.1080/21663831.2026.2659857

To link to this article: https://doi.org/10.1080/21663831.2026.2659857

MATER. RES. LETT.
https://doi.org/10.1080/21663831.2026.2659857

MATERIALS RESEARCH LETTERS
Taylor & Francis by informa

ORIGINAL REPORT

OPEN ACCESS Check for updates

Synchrotron-based nano-CT insights into microscale mechanics of sintered copper nanoparticles

Jiajie Fan [a,b,c], Xuyang Yan[a], Chuantong Chen[d], Leiming Du[b], Zichuan Li[b], Junran Zhang[c], Willem Van Driel[b] and Guoqi Zhang[b]

[a]Shanghai Engineering Technology Research Center of SiC Power Device, College of Intelligent Robotics and Advanced Manufacturing, Fudan University, Shanghai, People's Republic of China ; [b]EEMCS Faculty, Delft University of Technology, Delft, the Netherlands; [c]Research Institute of Fudan University in Ningbo, Ningbo, People's Republic of China; [d]Flexible 3D System Integration Laboratory, SANKEN, Osaka University, Osaka, Japan

ABSTRACT

Sintered Cu nanoparticles (Cu NPs) are promising interconnection materials for high-temperature power electronics, yet how their authentic three-dimensional pore architecture governs microscale deformation remains unclear. Here, synchrotron nano-computed tomography (nano-CT) was combined with in-situ micropillar compression, explicit dynamic elastoplastic finite element analysis, and TEM/TKD characterization to interrogate sintered Cu NPs. The nano-CT voxel size was 45 nm, and the reconstructed volume corresponded to a cylinder 16 μm in diameter and 10 μm in height. The average sectional porosity was 12.44%, with a systematic discrepancy between two-dimensional and three-dimensional porosity quantification. During loading, the porosity decreased to 9.55% while the pore aspect ratio increased from 1.82–2.35. Finite element analysis further showed pronounced pore-adjacent stress/strain localization at the elastic–plastic transition, with local stress and equivalent plastic strain reaching 650 MPa and 1.7×10^{-2}, compared with 250 MPa and 1.1×10^{-3} in adjacent regions. The GND density increased by 95.9% at a compressive strain of 26%, linking pore-induced strain gradients to dislocation accumulation. These results quantitatively connect authentic three-dimensional pore architecture, local deformation localization, and dislocation-mediated strengthening in sintered Cu NPs.

ARTICLE HISTORY
Received 4 December 2025

KEYWORDS
Synchrotron; X-ray nano-computed tomography; sintered Cu nanoparticles; microscale mechanical behavior; 3D reconstruction

Highlights

- Synchrotron nano-CT (45 nm voxel size) reconstructed a 16 × 10 μm cylindrical volume of sintered Cu NPs and resolved the authentic 3D pore network.
- Sectional porosity was 12.44%, and 2D/3D quantification showed a systematic discrepancy, with porosity decreasing to 9.55% and pore aspect ratio increasing from 1.82 to 2.35 during compression.
- Pore-adjacent localization was quantified at the elastic–plastic transition, with local stress/PEEQ reaching 650 MPa and 1.7×10^{-2} versus 250 MPa and 1.1×10^{-3} in adjacent regions.
- A 95.9% increase in GND density at 26% compressive strain links pore-induced strain gradients to dislocation accumulation and strain-gradient-driven strengthening.

1. Introduction

The rapid development of wide-bandgap power devices has imposed stringent reliability requirements on interconnection materials operating under high temperatures, large currents, and severe thermal cycling conditions [1]. Sintered copper nanoparticles (Cu NPs) have emerged as one of the most promising candidates to replace conventional solder owing to their high thermal conductivity, high melting point, and excellent resistance to electromigration [2,3]. However, the long-term reliability of sintered Cu NPs is strongly governed by their intrinsic microstructural features. Pore morphology, distribution,

CONTACT Xuyang Yan xyyan22@m.fudan.edu.cn Shanghai Engineering Technology Research Center of SiC Power Device, College of Intelligent Robotics and Advanced Manufacturing, Fudan University, Shanghai 200433, People's Republic of China

Supplemental data for this article can be accessed online at https://doi.org/10.1080/21663831.2026.2659857.

and connectivity not only dictate the static mechanical response but also strongly influence failure modes under thermal aging and fatigue conditions [4–6]. Previous studies have experimentally evaluated the mechanical behavior of sintered Cu NPs, but mechanistic explanations remain limited [7,8]. Thus, achieving an in-depth understanding and accurate characterization of their three-dimensional (3D) microstructure is essential for assessing both mechanical performance and service reliability.

Current characterization techniques, however, remain insufficient. Conventional two-dimensional microscopy provides only sectional information and fails to capture authentic 3D pore networks [9–11]. Computational approaches, such as quartet structure generation set algorithm [12] and molecular dynamics simulations [6,9,13], have been employed to construct virtual sintered structures, yet they cannot reproduce the morphological complexity and spatial distribution of real pores. Serial sectioning by focused ion beam (FIB) offers higher resolution reconstructions but is destructive, expensive, and time-consuming, restricting its applicability [14]. Consequently, an efficient, non-destructive method is still lacking, which limits reliable input for microstructure-dependent studies spanning electrical, thermal, mechanical, and reliability domains.

Synchrotron-based X-ray nano-computed tomography (nano-CT) offers a promising solution to this challenge. Compared with conventional micro-CT, nano-CT achieves higher resolution while maintaining high throughput and non-destructive imaging [15,16]. In contrast to FIB-based sectioning, it avoids labor-intensive sample preparation and destructive milling, enabling rapid and faithful reconstruction of the pore network [17,18]. Although nano-CT has already been applied to porous metallic systems [19], and microscale in-situ mechanical studies on sintered Cu-based materials have also been reported [7,8], these efforts have rarely been integrated to directly correlate the authentic three-dimensional pore architecture of sintered Cu NPs with their pore-controlled local deformation behavior. Unlike prior studies that focus on surface or post-mortem analysis, this work directly quantifies porosity evolution during in-situ compression.

This study combines synchrotron nano-CT, in-situ micropillar compression, explicit dynamic elastoplastic finite element analysis, and TEM/TKD characterization to interrogate how the authentic three-dimensional pore architecture of sintered Cu NPs governs local deformation. Specifically, it quantifies the discrepancy between sectional and volumetric porosity, characterizes pore-adjacent stress/strain localization during compression, and links the resulting local strain gradients to geometrically necessary dislocation (GND) accumulation and strengthening. The study thus establishes a direct structure—deformation—strengthening correlation for sintered Cu NPs and provides a quantitative framework for understanding pore-controlled micromechanical behavior.

2. Methodology

3D microstructural reconstruction of sintered Cu NPs was performed at the BL18B beamline of the Shanghai Synchrotron Radiation Facility (SSRF) using full-field transmission X-ray microscopy (TXM) [20]. A bending-magnet source provided hard X-rays, and the setup (Figure 1(a)) incorporated an ellipsoidal monocapillary condenser, a Fresnel zone plate objective, and an sCMOS-based detector system. Nano-tomography was carried out at 8.4 keV with an effective voxel resolution of $\sim$45 nm. Each dataset was collected from 360 projections between 0° and 180° at a step size of 0.5° and an exposure time of 1.5 s. Segmentation of the pore network was conducted in Avizo, where a watershed-based thresholding method was employed to delineate pores from the metallic matrix (Figure 1(b)). Quantitative analysis provided 2D and 3D pore morphology, which were subsequently used for explicit dynamic elastoplastic finite element analysis.

The detailed material composition and formulation of the slurry system used in this study were previously established [21]. Sintered Cu NPs were fabricated by pressure-assisted sintering (Sinterstar Auto-F-XL-HC, Boschman) at 250°C and 20 MPa for 3 mins under nitrogen [7]. The sintered layer used in this study had been previously verified to possess good uniformity and consistency [7]. In-situ micropillar compression tests were performed using a dual-beam FIB-SEM (Helios 5 DualBeam, Thermo Fisher Scientific) equipped with a nano-indentation system [7]. In-situ mechanical tests were performed in micropillar compression mode under continuous loading at a strain rate of 0.006 s^{-1}. TEM characterization was conducted in an aberration-corrected transmission electron microscope (Spectra 300, Thermo Fisher Scientific). Explicit dynamic finite element simulations of micropillar compression were implemented in ABAQUS/Explicit 2021.

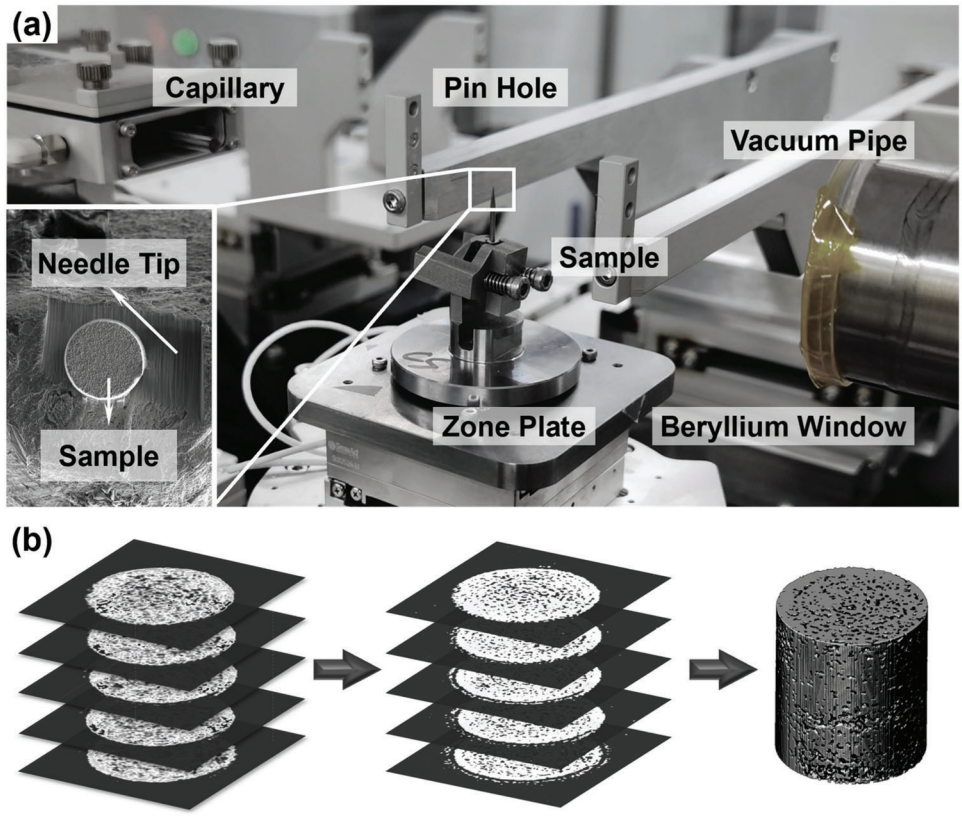

Figure 1. (a) Experimental setup of the synchrotron-based nano-CT; (b) 3D geometric reconstruction of sintered Cu NPs.

3. Results and discussion

3.1. 3D microstructural reconstruction of sintered Cu NPs

Synchrotron-based nano-computed tomography (nano-CT) was employed to achieve non-destructive 3D reconstruction of sintered Cu NPs, thereby providing direct insight into their intrinsic microstructural features. The reconstructed volume encompassed a cylindrical specimen with a diameter of 16 µm and a height of 10 µm, as shown in Figure 2(a). To validate the reconstruction, a representative XY section extracted from the 3D nano-CT dataset was compared with an FIB-prepared cross-section from the same specimen, as shown in Figure 2(b). Although the two sections were not taken from exactly the same spatial location, they showed comparable pore characteristics, and the porosity measured from the FIB cross-section (12.99%) closely matched the average sectional porosity extracted from the 3D dataset (12.44%), supporting the reliability of the nano-CT reconstruction.

To further probe local variations, five micropillars (labeled a–e) were virtually sectioned from the reconstructed volume. Each micropillar had a diameter of 3 µm and a height of 7.5 µm, and they were extracted at intervals of 2 µm along the Z-axis of the sintered body. The two-dimensional relative density of each micropillar was evaluated slice by slice along its height direction (Z-axis), as shown in Figure 2(e,f). The average sectional relative densities of micropillars a–e ranged from 0.812–0.892, compared with a global average sectional value of 0.875. Linear fitting of the relative density trends revealed slopes ranging from -2.58×10^{-4} to 4.62×10^{-4}, indicating that the overall microstructure of the sintered body exhibited no significant porosity gradient along the pressing direction. Instead, the porosity remained broadly uniform at the mesoscale, while individual micropillars exhibited larger sectional fluctuations owing to their smaller sampling volumes and thus greater sensitivity to local structural variations.

In addition, the average sectional porosity of micropillars a–e did not show any systematic trend with respect to their spatial positions in the XY plane, as presented in Figure 2(f), indicating similar porosity levels across the lateral positions. In contrast, volumetric analysis gave 3D relative densities of 0.779–0.892 for micropillars a–e and an overall 3D average of 0.816, lower than the average sectional value of 0.875. This quantitative difference demonstrates that two-dimensional sectional analysis tends to overestimate relative density and thus underestimate the

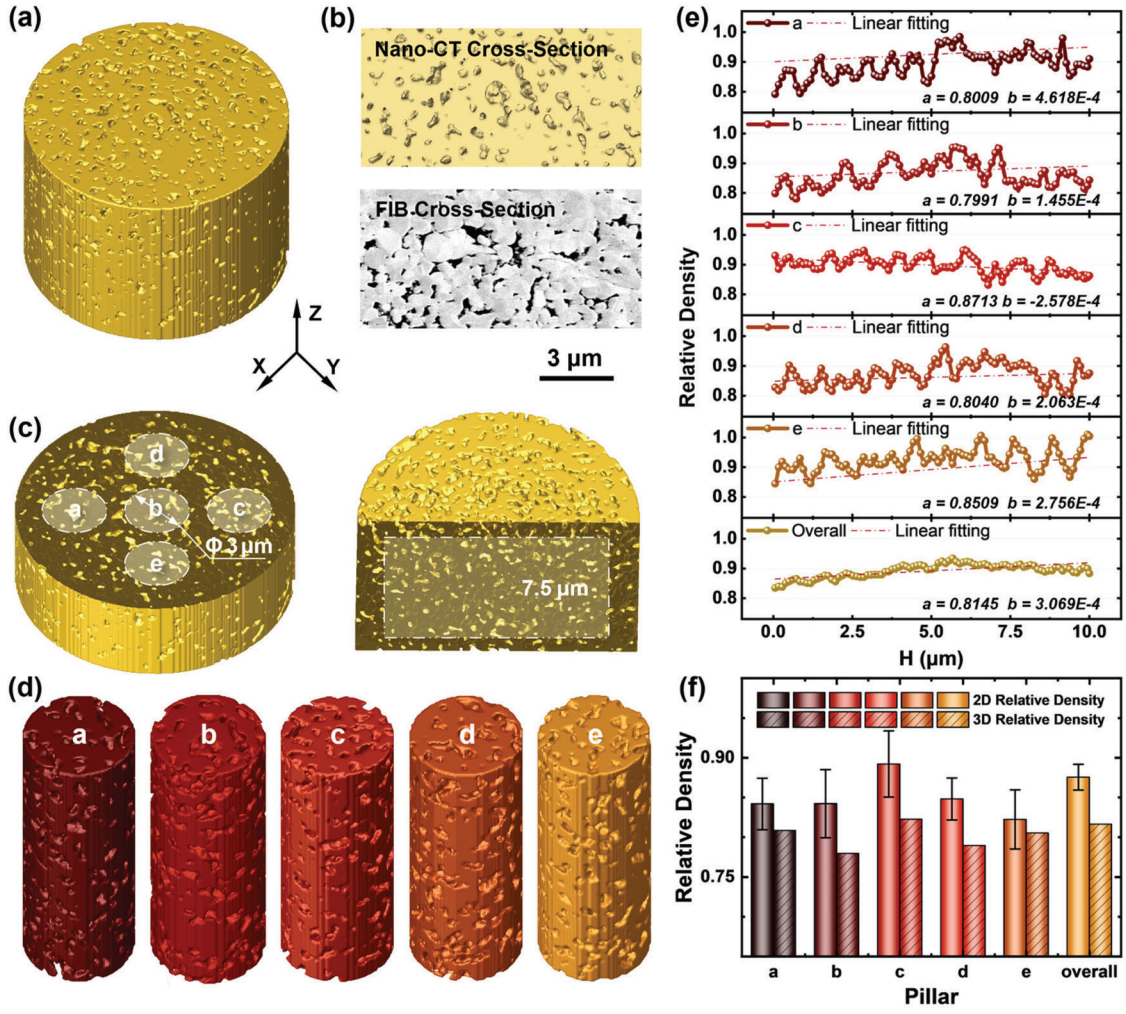

Figure 2. 3D reconstruction and analysis of sintered Cu NPs by synchrotron nano-CT. (a) Overall 3D reconstructed volume. (b) Comparison between a representative nano-CT sectional porosity map and an FIB-prepared cross-section. (c) Locations and dimensions of micropillars a–e. (d) Morphologies of micropillars. (e) Variation of sectional relative density. (f) Average sectional relative density.

true void fraction in the sintered Cu NP structure. Similar discrepancies between two-dimensional and three-dimensional porosity evaluation have also been reported in previous studies [22].

In summary, synchrotron nano-CT enabled a comprehensive 3D reconstruction of sintered Cu NPs, revealing clear quantitative differences between sectional and volumetric porosity while also capturing local pore fluctuations at the micropillar scale.

3.2. Microscale mechanistic insights from FEM—experiment integration

The constitutive response of sintered Cu NPs under compression was established based on engineering stress–strain curves obtained from in-situ micropillar compression tests. An elastoplastic constitutive law was derived and subsequently implemented in finite element simulations of micropillars a–e, which were virtually extracted from the nano-CT reconstructed volume, as shown in Figure 3. The simulated stress–strain curves captured the essential features of the experimental response, thereby validating the accuracy of the constitutive model for describing the compressive behavior of sintered Cu NPs at the microscale (Figure 4(a)).

The TEM/SAED results for the pre-sintered, sintered, and compressed states (Figure 5) indicate that the material remains predominantly FCC Cu throughout the process, without distinct copper-oxide diffraction features. Consistently, EDX analysis (Figs. S1–S3 and Tables S1–S3) shows only low oxygen contents, while the higher pre-sintering C signal markedly decreases after sintering due to the removal of residual organics or surface adsorbates.

Morphological evolution (Figure 3(a–h)) revealed that both experiment and simulation exhibited pronounced

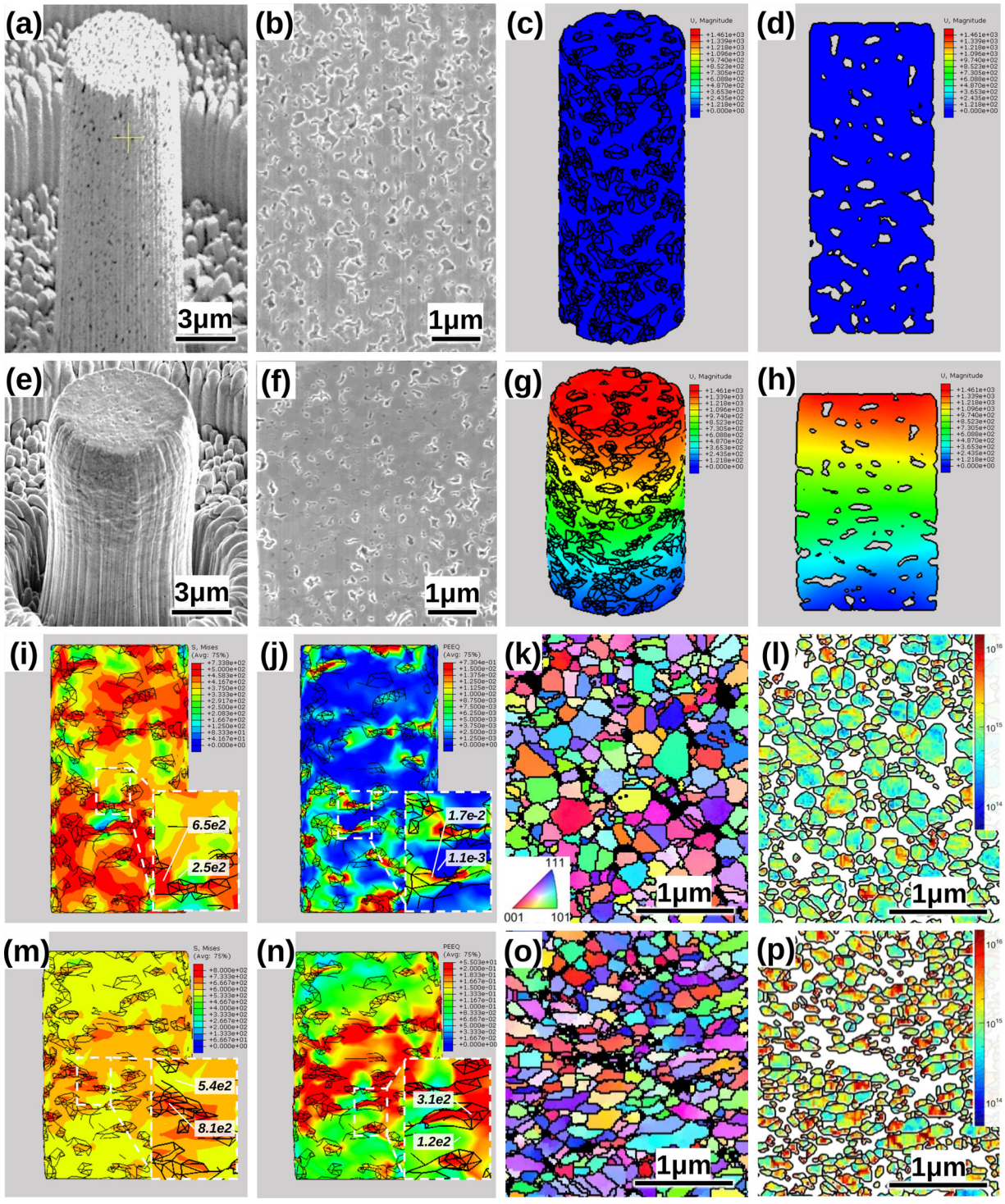

Figure 3. Experimental and simulated results of sintered Cu NPs micropillar compression. (a–h) Morphological evolution: (a, e) SEM morphologies; (b, f) SEM cross-sections; (c, g) FEM models reconstructed from nano-CT; (d, h) FEM sections. (i–n) Evolution of stress and strain fields from the elastic–plastic transition to the plastic deformation stage: (i, m) stress distributions; (j, n) equivalent plastic strain (PEEQ) distributions. (k–p) Crystallographic characterization by TKD: (k, o) inverse pole figures; (l, p) dislocation-density distributions.

plastic deformation when compressed to 26% (experiment) and 24% (simulation), forming a barrel-shaped profile indicative of excellent plasticity in the sintered Cu NPs. To quantitatively relate the mechanical response to the structural evolution, the porosity and pore aspect ratio were statistically analyzed during compressive loading, as shown in Figure 4(b). The porosity decreased from 12.44% before compression to 9.55% after loading, while the average pore aspect ratio increased from 1.82–2.35. These results indicate that, as the applied compressive

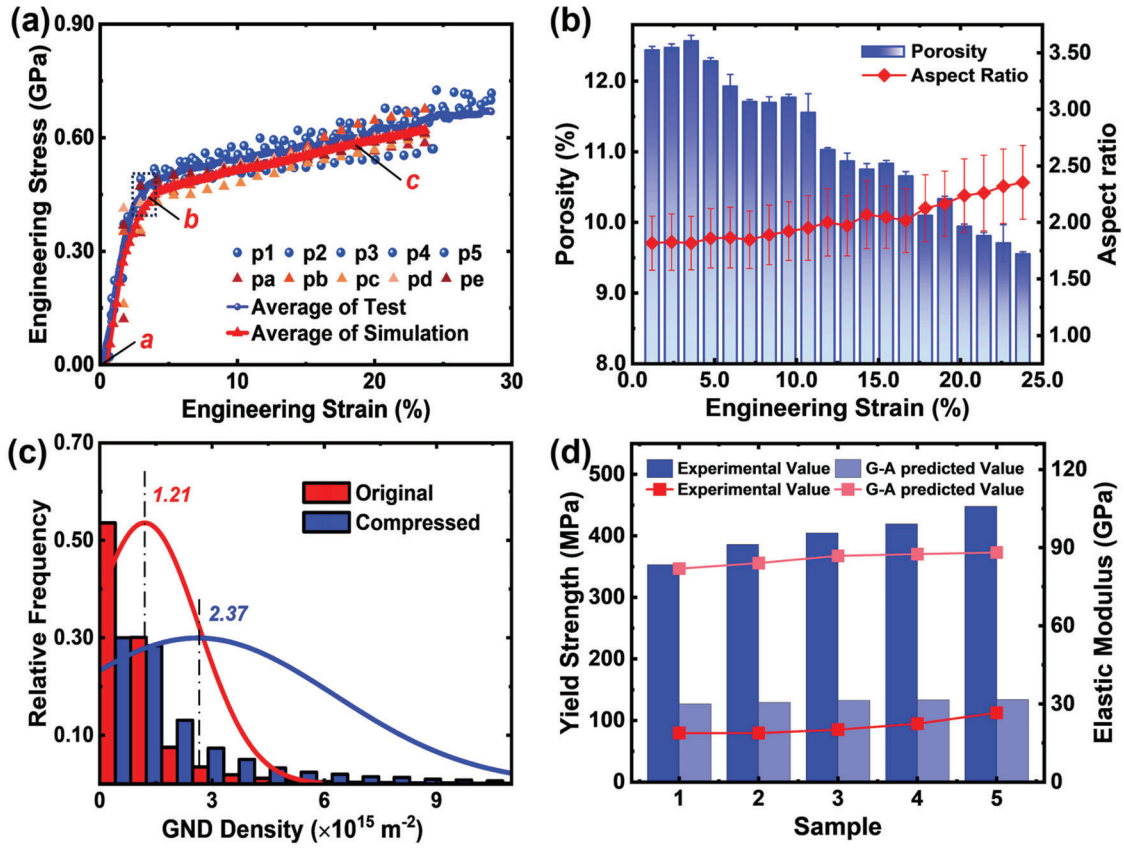

Figure 4. Mechanical response and pore evolution during compression of sintered Cu NPs. (a) Stress–strain curve; (b) Porosity and pore aspect ratio; (c) GND density evolution; (d) Gibson–Ashby prediction versus experiment.

stress increased, internal pores progressively closed and the remaining pores became more elongated. During deformation, small pores gradually closed, whereas larger pores elongated and deformed, consistent across SEM and FEM observations.

At the elastic–plastic transition (point b in Figure 4(a)), the von Mises stress maps (Figure 3(i)) show pronounced pore-adjacent stress localization. In the local magnified view, the concentrated region reaches 650 MPa, whereas the adjacent region remains at 250 MPa. Consistently, the PEEQ contours in Figure 3(j) reveal early strain localization near the pores, with local values of 1.7×10^{-2} compared with 1.1×10^{-3} in the adjacent region. These quantitative results support pore-scale stress/strain localization during the elastic–plastic transition and are consistent with the early closure of nearby small pores observed experimentally (Figure 3(b)). Upon entering the plastic regime (point c), the stress field becomes more broadly distributed but remains concentrated in the central region (Figure 3(m)), accompanied by a clearer specimen-scale strain-gradient pattern. This may help explain the earlier pore closure observed in the mid-section relative to the top and bottom regions. The nano-CT-based FEM results thus provide a quantitative basis for understanding the strain-localization behavior observed in the in-situ experiments.

At the microscale, TEM and TKD characterizations confirmed these findings. The geometrically necessary dislocation (GND) density increased 95.9%, from 1.21×10^{15} m^{-2} before compression to 2.37×10^{15} m^{-2} afterward. This increase aligns with the strain-gradient fields predicted by FEM, suggesting that pore-induced strain gradients may play an important role in GND formation. TEM observations of the as-prepared, sintered, and compressed states (Figure 5) show well-developed sintering necks but no obvious post-compression debonding or neck fracture. Instead, the post-compression microstructure is characterized by pore collapse/elongation and occasional thin micro-cracks near incompletely collapsed void boundaries, consistent with localized plastic collapse rather than debonding- or neck-fracture-dominated separation. These observations suggest that strain-gradient-driven GND generation and accumulation are important contributors to the strengthening behavior of sintered Cu NPs [23].

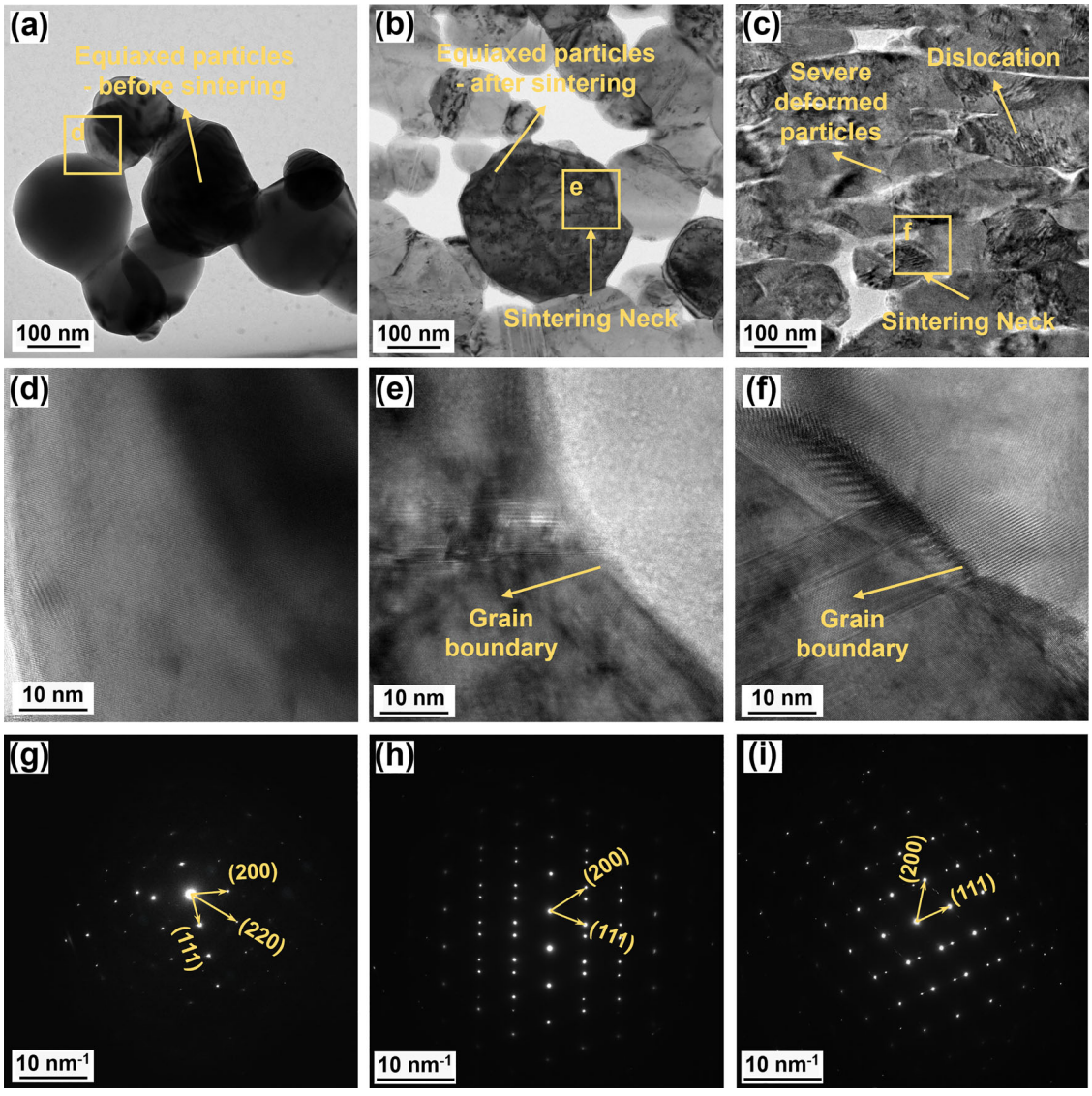

Figure 5. TEM characterization of sintered Cu NPs pre-sintered, sintered and after compression. (a–c) TEM images; (d–f) HRTEM images; (g–i) SAED patterns.

Comparison with the Gibson–Ashby model [24,25] shows overpredicted modulus but underpredicted strength (Figure 4(d)), indicating a clear deviation from the response of traditional metallic foams and supporting the strain-gradient-driven strengthening mechanisms identified here.

In summary, the explicit dynamic simulations based on synchrotron nano-CT effectively uncover the pore-induced strain-gradient–driven dislocation strengthening mechanism of sintered Cu NPs that has been observed experimentally but remained difficult to explain [7].

4. Conclusion

This work establishes a synchrotron nano-CT-based framework for linking the three-dimensional pore architecture of sintered Cu nanoparticles to their microscale compressive deformation. By integrating non-destructive 3D reconstruction, in-situ micropillar compression, finite element analysis, and TEM/TKD characterization, it is shown that pore morphology is closely associated with local plastic deformation, strain-gradient evolution, and GND accumulation during compression. The results therefore provide a microstructure-informed understanding of the interplay between pore evolution and dislocation-mediated strengthening in sintered Cu nanoparticle structures.

This study also has several limitations. The nano-CT analysis is constrained by spatial resolution and acquisition conditions, and the reconstructed volume represents only a finite region rather than the entire sintered layer. Direct identification of internal load-transfer pathways requires DVC or equivalent full-field

techniques and is beyond the scope of this study. In addition, the present work focuses on microscale compressive behavior and does not directly address tensile, fatigue, thermal-cycling, or long-term reliability responses. Accordingly, the present framework should be regarded as a microstructural and mechanistic basis for future reliability-oriented studies, rather than a direct substitute for dedicated reliability evaluation.

Acknowledgements

We sincerely thank the Shanghai Synchrotron Radiation Facility of BL18B (https://cstr.cn/31124.02.SSRF.BL18B) for the assistance on Nano-CT.

Author contributions

CRediT: **Jiajie Fan:** Conceptualization, Formal analysis, Funding acquisition, Investigation, Methodology, Project administration, Resources, Software, Supervision, Validation, Writing – original draft, Writing – review & editing; **Xuyang Yan:** Data curation, Formal analysis, Investigation, Validation, Writing – original draft; **Chuantong Chen:** Supervision; **Leiming Du:** Writing – review & editing; **Zichuan Li:** Writing – review & editing; **Junran Zhang:** Funding acquisition, Project administration, Resources; **Willem Van Driel:** Supervision; **Guoqi Zhang:** Resources, Software, Supervision

Disclosure statement

No potential conflict of interest was reported by the authors .

Funding

The work described in this paper was supported by the National Natural Science Foundation of China [grant number 52275559], China Scholarship Council [grant number 202406100064] and Zhejiang Provincial Natural Science Foundation of China [grant number LQN25F040015].

ORCID

Jiajie Fan http://orcid.org/0000-0001-5400-737X

References

[1] Wei JX, Wei ZX, Fu H, et al. Review on the reliability mechanisms of SiC power MOSFETs: a comparison between planar-gate and trench-gate structures. IEEE Trans Power Electron. 2023;38(7):8990–9005. doi:10.1109/TPEL.2023.3265864

[2] Chen TF, Siow KS. Comparing the mechanical and thermal-electrical properties of sintered copper (Cu) and sintered silver (Ag) joints. J Alloys Compd. 2021;866:158783. doi:10.1016/j.jallcom.2021.158783

[3] Wang YJ, Xu D, Yan HD, et al. Low-temperature copper sinter-joining technology for power electronics packaging: A review. J Mater Process Technol. 2024;332:118526. doi:10.1016/j.jmatprotec.2024.118526

[4] Du LM, Jiao WP, Bäcke O, et al. Interface strength and crack propagation mechanisms in sintered copper nanoparticles. Acta Mater. 2025 Sep;296: 121187. doi:10.1016/j.actamat.2025.121187.

[5] Bhogaraju SK, Mokhtari O, Conti F, et al. Die-attach bonding for high temperature applications using thermal decomposition of copper(II) formate with polyethylene glycol. Scr Mater. 2020;182:74–80. doi:10.1016/j.scriptamat.2020.02.045

[6] Du LM, Liu K, Hu D, et al. Microstructural and mechanical anisotropy in pressure-assisted sintered copper nanoparticles. Acta Mater. 2025;287:120772. doi:10.1016/j.actamat.2025.120772

[7] Yan X, Du L, Gu C, et al. Microscale mechanical properties in sintered copper nanoparticles. Mater Sci Eng A. 2025;943:148684. doi:10.1016/j.msea.2025.148684

[8] Son S, Lee JW, Asghari-Rad P, et al. Hierarchically heterogeneous microstructure and mechanical behavior of the multi-materials prepared by powder severe plastic deformation. Mater Res Lett. 2023;11(11):915–924. doi:10.1080/21663831.2023.2258158

[9] Yang S, Kim W, Cho M. Molecular dynamics study on the coalescence kinetics and mechanical behavior of nanoporous structure formed by thermal sintering of Cu nanoparticles. Int J Eng Sci. 2018;123:1–19. doi:10.1016/j.ijengsci.2017.11.008

[10] Sun S, Wang W, Zhang C, et al. Synthesis and mechanical properties of low crack-density bulk hierarchical nanoporous copper. Scr Mater. 2025;258:116531. doi:10.1016/j.scriptamat.2024.116531

[11] Zhang Z, Chen C, Suetake A, et al. Pressureless and low-temperature sinter-joining on bare Si, SiC and GaN by a Ag flake paste. Scr Mater. 2021;198:113833. doi:10.1016/j.scriptamat.2021.113833

[12] Liu W, Wang X, Zhang J, et al. Quartet structure generation set algorithm based 3D reconstruction on porous structures of sintered copper joints for power electronics packaging. Scr Mater. 2025;265:116750. doi:10.1016/j.scriptamat.2025.116750

[13] Engelman B, Mathesan S, Fedyaeva T, et al. Deformation behavior of nanoporous gold nanoparticles during compression. Acta Mater. 2025 Mar;286: 120723. doi:10.1016/j.actamat.2025.120723.

[14] Hu X, Martin HA, Poelma R, et al. Exploring the process-microstructure-thermal properties relationship of resin-reinforced Ag sintering material for high-power applications via 3D FIB-SEM nanotomography. Mater Des. 2024;244:113185. doi:10.1016/j.matdes.2024.113185

[15] Chen RC, Liu P, Xiao TQ, et al. X-ray imaging for non-destructive microstructure analysis at SSRF. Adv Mater. 2014;26(46):7688–7691. doi:10.1002/adma.201402956

[16] Sang D, Luo X, Liu J. Biological interaction and imaging of ultrasmall gold nanoparticles. Nano-Micro Lett. 2024;16(1):44. doi:10.1007/s40820-023-01266-4

[17] Li K, Xie H-L, Fu Y-N, et al. Fast X-ray imaging beamline at SSRF. Nucl Sci Tech. 2024;35(9):154. doi:10.1007/s41365-024-01488-0

[18] Tao F, Tian N, Wang J, et al. Enhancing full-field TXM with low emittance synchrotron sources: monocapillary condenser shaker optimization. Rev Sci Instrum. 2025;96(5):053702. doi:10.1063/5.0256187

[19] Xu R, Lu YM, Dai YT, et al. Simultaneous improvement of mechanical strength and electrical conductivity in Al-2.5 wt% Fe alloy rods with high thermal stability by high-pressure torsion extrusion. Mater Charact. 2025 Jun;224:114956. https://doi.org/10.1016/j.matchar.2025.114956.

[20] Zhang L, Tao F, Wang J, et al. The 3D nanoimaging beamline at SSRF. Nucl Sci Tech. 2023;34(12):201. doi:10.1007/s41365-023-01347-4

[21] Liu X, Li SZ, Fan JJ, et al. Microstructural evolution, fracture behavior and bonding mechanisms study of copper sintering on bare DBC substrate for SiC power electronics packaging. J Mater Res Technol. 2022;19:1407–1421. doi:10.1016/j.jmrt.2022.05.122

[22] Karlova P, Serdechnova M, Blawert C, et al. Comparison of 2D and 3D plasma electrolytic oxidation (PEO)-based coating porosity data obtained by X-ray tomography rendering and a classical metallographic approach. Materials (Basel). 2022;15(18):6315. doi:10.3390/ma15186315

[23] Edalati K, Bachmaier A, Beloshenko VA, et al. Nanomaterials by severe plastic deformation: review of historical developments and recent advances. Mater Res Lett. 2022;10(4):163–256. doi:10.1080/21663831.2022.2029779

[24] Yan C, Hao L, Yang L, et al. Chapter 3 - metal alloys uniform TPMS structures. In: Yan C, Hao L, Yang L, et al., editors. Triply periodic minimal surface lattices additively manufactured by selective laser melting. London, UK: Academic Press; 2021. p. 39–130. doi: 10.1016/B978-0-12-824438-8.00003-0.

[25] Hodge AM, Wang YM, Barbee TW. Large-scale production of nano-twinned, ultrafine-grained copper. Mater Sci Eng A. 2006;429(1-2):272–276. doi:10.1016/j.msea.2006.05.109